ORIGINAL ARTICLE

TRANSPORT PHENOMENA AND FLUID MECHANICS

Method of mass production of monodisperse microbubbles aided by intense pressure gradients

Enrique S. Quintero[1] | **Jose Manuel Gordillo**[1]

[1]Universidad de Sevilla

Correspondence

Área de Mecánica de Fluidos, Departamento de Ingenería Aeroespacial y Mecánica de Fluidos, Universidad de Sevilla, Avenida de los Descubrimientos s/n 41092, Sevilla, Spain.

Email: jgordill@us.es

Present address

Área de Mecánica de Fluidos, Departamento de Ingenería Aeroespacial y Mecánica de Fluidos, Universidad de Sevilla, Avenida de los Descubrimientos s/n 41092, Sevilla, Spain.

Funding information

Spanish MINECO under Project DPI2017-88201-C3-1-R, partly financed through European funds.

Here we present a method for producing non-coalescing monodisperse microbubbles in an efficient, massive and controlled way. Since our prototype is easily scalable, it can be straightforwardly adapted to satisfy the specific gas injection demands required by the different applications where it can be used, like bioreactors or water treatment or purification plants. The main feature of the bubbling device described here consists of injecting the gas at the leading edge of a wing in relative motion with respect to a liquid. The reasons for this particular design relies on the smallness of the drag coefficient of streamlined bodies and also on the fact that the strongest favourable pressure gradients and the minimum values of the liquid pressures are located at the leading edge of the airfoils composing the wing.

Keywords —Bubble formation; Microbubble; Bubble coalescence; Water treatment; Bioreactor

1 | INTRODUCTION

A wide variety of applications, among which one could cite waste water treatment and water purification [1–3], syngas fermentation and biomass processing [4–6], particle separation (see, e.g. [7] and references therein), the cleaning of surfaces [8], lithotripsy [9] or drug delivery [10] rely on the dispersion of bubbles in a flow. It is well known that the performance of the different processes enumerated above can be notably improved by decreasing the diameters of the bubbles produced [11,12], a fact explaining the continuous stream of contributions in the recent literature aimed at describing different methods of production of microbubbles [13]. For instance, in bioreactors, the mass transfer process of oxygen is largely favoured when the diameters of the bubbles is reduced. Indeed, when bubble size is decreased, the contact area per unit volume of gas increases, as well as the residence time of bubbles in the reactor. In addition, since the concentration gradients are also larger because of the higher Laplace pressure, the mass flux per unit area of gas-liquid interface also increases.

The simplest method of generation, which consists of directly injecting the gas from an orifice or nozzle into a stagnant liquid pool, is not of practical use in applications because the diameters of the bubbles produced in this way are substantially larger than the size of the injector from which they are generated [14,15]. In addition, this method also favors the coalescence between neighbouring bubbles for sufficiently high values of the gas flow rate [15,16]. These undesirable effects are avoided by using surfactants and by injecting the gas within a liquid coflow or a crossflow, which help increase the distance between consecutive bubbles [13]. These strategies are, in fact, implemented in modern bubbling devices, where both the liquid and the gas are forced to flow through micron-sized channels [17–21]. In this way, novel microfluidic technologies are capable to produce, at rates of $\sim 10^5$ Hz and from just a single orifice, uniform-sized bubbles with diameters comparable with a red blood cell ($\sim 5\,\mu m$) which, when stabilized with a biocompatible phospholipid shell, can be used as ultrasound contrast agents (UCAS), see e.g. [22–24]. However, microfluidic devices

cannot be employed in most of the processes in chemical industry because of the fact that microchannels are prone to clogging by particles or other impurities and also because of the high energy consumption associated with the large pressure losses needed to make the fluids flow through the micron-sized constrictions. It is precisely the purpose of this contribution to present an easily scalable prototype designed to inject monodisperse microbubbles in biorreactors or in water purification processes which avoids the main problems associated with the use of micron-sized geometries, i.e. very limited production rates, clogging and large power consumption.

Next section is devoted to provide the theoretical ideas used in the design of the prototype tested in section 3 and the main results are summarized in section 4.

2 | THEORETICAL BACKGROUND

In this section we deduce scaling relationships for the bubbling frequency f_b and for the bubble diameter d_b as a function of the control parameters. For that purpose, we make use of the fact that, thanks to the smallness of the gas to liquid density and viscosity ratios, the gas dynamical effects can be safely neglected during most of the bubble formation process[13]. This approach will be valid until the last few microseconds prior to pinch-off: it is only during this very short period of time that the gas pressure gradients are large enough to modify the dynamics of the liquid implosion process[25]. Then, with the only purpose of scaling f_b and d_b as a function of the gas flow rate Q_g and of the characteristic liquid velocity U, the formation of a bubble can be viewed, in the limit of high Reynolds numbers of interest here, as the inertial collapse of a void of diameter d_b surrounded by a liquid of density ρ in a characteristic time f_b^{-1}. Therefore, assuming that the inertial implossion of the void is caused by the pressure difference Δp,

$$\rho d_b^2 f_b^2 \sim \Delta p\,, \tag{1}$$

with the analogous balance for the case in which the collapse is dominated by liquid viscosity, given in [26]. Since the pressure in the gas is uniform inside the bubble, Δp in equation (1) represents the pressure difference between two points at the liquid side of the interface separated by a distance $\propto d_b$. Consequently,

$$\Delta p \propto |\nabla p| d_b + k\sigma/d_b = |\nabla p| d_b \left(1 + k\frac{\sigma}{|\nabla p| d_b^2}\right), \tag{2}$$

with k a prefactor of order unity, $|\nabla p|$ the modulus of the pressure gradient and σ indicating the interfacial tension coefficient [13,26]. Then, in view of equations (1)-(2), if the Bond number, defined here as $Bo = |\nabla p| d_b^2/\sigma$, verifies the condition

$$Bo = \frac{|\nabla p| d_b^2}{\sigma} \gtrsim O(1), \tag{3}$$

the substitution of equation (2) into (1) yields:

$$f_b \propto \sqrt{\frac{|\nabla p|}{\rho\, d_b}}\,. \tag{4}$$

In addition, since the gas flow rate Q_g can be expressed as a function of f_b and d_b as

$$Q_g = \frac{\pi}{6} d_b^3 f_b\,, \tag{5}$$

the substitution of f_b in (4) into equation (5) provides with the following scaling relationship:

$$d_b^3 \sqrt{\frac{|\nabla p|}{\rho\, d_b}} \propto Q_g \Rightarrow d_b \propto \left(\frac{Q_g}{\sqrt{|\nabla p|/\rho}} \right)^{2/5} . \tag{6}$$

For equations (4)-(6) to be valid, the pressure gradient needs to be favourable i.e., the pressure needs to decrease in the streamwise direction because, otherwise, bubbles would coalesce, as it was shown in [27]. Notice that, for the particular case in which bubbles are formed within a quiescent liquid as it is depicted in figure 1a, $|\nabla p| = \rho\, g$ and, hence, equation (6) recovers the expression for the bubble diameter already deduced in [14]. However, as it was pointed out above, the bubbles produced in this way are far larger than the size of the injector [15]. Then, in order to reduce the diameters of the bubbles produced, we take advantage of the fact that equations (4)-(6) express that the bubbling frequency increases and the bubble diameter decreases when $|\nabla p|$ increases. Therefore, the strategy we proposed in [26,27] to produce micron-sized bubbles at high rates was to inject the gas in a region of the flow where $|\nabla p|/(\rho\, g) \gg 1$. In [26], the gas is injected at the entrance region of a tube, where the flow accelerates from rest up to a velocty $U \sim 1$ ms^{-1} in a characteristic length $L = 10^{-3}$ m -see figure 1b, so in this case $|\nabla p|/(\rho\, g) \sim U^2/(g\, L) \sim O(10^2)$. In [27], the gas is injected at the leading edge of an airfoil at an angle of attack α with respect to the incoming free stream of velocity U_∞, see figures 1c and 2. In this case, there also exists a very strong favourable pressure gradient at the point where bubbles are generated because the pressure changes from the maximum value at the stagnation point, $p_\infty + 1/2\rho U_\infty^2$, to the minimum value at the suction peak, in a distance which is much smaller than the chord c (see figures 1c and 2). Then, defining the pressure coefficient as

$$C_p = \frac{p - p_\infty}{\rho U_\infty^2/2} , \tag{7}$$

the pressure gradient at $x/c = 0$, namely, at the leading edge of the airfoil -see figures 1c and 2- can be expressed as

$$|\nabla p| = \beta(\alpha)\frac{\rho U_\infty^2}{c} \tag{8}$$

with

$$\beta(\alpha) = -\frac{1}{2}\frac{\mathrm{d}C_p}{\mathrm{d}\bar{s}}(\alpha, x/c = 0) \gg 1 \tag{9}$$

the positive value of the (favourable) dimensionless pressure gradient and $s = \bar{s}c$ indicating the arclength along the airfoil surface (see figures 1c and 2). The numerical values of β, calculated in [27,28] solving the Laplace equation subjected to the impenetrability condition at the airfoil surface, reveals that $\beta(\alpha) \gtrsim O(10^2)$. Consequently, the value of the pressure gradient is, in this case, comparable with that created using microfluidic geometries [26] because $|\nabla p| \sim \rho\beta(\alpha) U_\infty^2/c \sim \rho U^2/L$, with $U_\infty \sim U$ and $c \gg L$, with L the indicating the constant length, $L = 10^{-3}$ m (see figures 1b-c). Then, non-coalescing monodisperse microbubbles can also be generated using meter-sized geometries, avoiding the inherent problems of microfluidics related with the clogging by particles and the high power consumption, thanks to the intense favourable pressure gradients existing at the leading edge of airfoils at an angle of attack $\alpha \neq 0$.

For the case considered in [27], bubbling frequencies and bubble diameters can be predicted once equations (8)-(9) are substituted into equations (4)-(6):

$$f_b = K_{f1}\left(\frac{U_\infty}{\sqrt{cd_b/\beta(\alpha)}}\right) \quad \text{and} \quad \frac{d_b}{L} = K_{b1}\left(\frac{Q_g}{U_\infty L^2\sqrt{L\beta(\alpha)/c}}\right)^{2/5}, \tag{10}$$

with $L = 10^{-3}$ m and with $K_{f1} = 1.8$ and $K_{b1} = 1.11$ constants which do not depend on the geometry. Indeed, we showed in [27] that the values of K_{f1} and K_{b1} in equations (10) for the aerator depicted in figure 1c are the same as in the case of the bubble maker depicted in figure 1b. Consequently, the results in [27] support the validity of equations (4)-(6) in general types of flows whenever the pressure gradient is favourable, viscous stresses are negligible -this is usually verified for low viscosity liquids such as water- and when $Bo \gtrsim O(1)$ -see equation (3), a condition which can be alternatively written as

$$\frac{|\nabla p|\ d_b^2}{\sigma} \gtrsim 1 \Rightarrow d_b \gtrsim \left(\frac{\sigma}{|\nabla p|}\right)^{1/2}. \tag{11}$$

For the typical values $\sigma \simeq 7 \times 10^{-2}$ Nm^{-1}, $\rho = 10^3$ Kgm^{-3}, $U_\infty \simeq 2$ ms^{-1}, $c \simeq 0.1$ m and $\beta \simeq 200$ (see [27] or the results in the next section), equations (10) can be used whenever equation (11) is verified namely, for bubble diameters satisfying the condition $d_b \gtrsim 100\,\mu m$, a value which could be clearly smaller if $U_\infty > 2$ ms^{-1}.

3 | DESIGN AND TEST OF A DEVICE TO MASSIVELY PRODUCE MONODISPERSE MICROBUBBLES

In this section we describe a prototype based on the previous ideas by [27] to produce microbubbles in pure water avoiding the coalescence between neighbours and the clogging by particles or other impurities. The idea behind the present design consists of injecting the gas through a plurality of orifices located at the leading edge of rectangular wings of chord c and span b, submerged at a depth H within a liquid reservoir, and placed at a distance R from an axis that rotates with an angular velocity Ω, see figure 3. Since the number N of injection orifices and the number of rotating wings can be easily increased, the present design can be used as an aeration and gas diffusion system capable of producing monodisperse microbubbles at industrial scale with the additional advantage of also being efficient from an energetical point of view. Indeed, this is because of the reduced drag coefficient of streamlined bodies when

boundary layer separation is prevented and because the gas is injected at the leading edge of the wing, where the liquid pressure is minimum. Then, since the liquid pressure at the leading edge of the rotating wing is

$$p_{local} - p_a = \rho\, g\, H + \frac{1}{2}\rho\,(\Omega\, R)^2\; C_p(x/c = 0)\,, \tag{12}$$

with p_a the atmospheric pressure, the pressure difference needed to make the gas flow along the injection system is reduced in

$$\frac{1}{2}\rho\,(\Omega\, R)^2\; |C_p(x/c = 0)|\,. \tag{13}$$

The substitution of the characteristic values $\Omega\, R \sim 2$ ms^{-1} and $C_p \simeq -4$ (see figure 4b-c) in equation (13) provides a reduction of the gas injection pressure of $\simeq 10^4$ Pa, a value that could be even larger for larger values of $\Omega\, R$ and of the angle of attack, α, as it will be shown next.

The values in table 1 of both the angle of attack $\alpha = 7^o$ and of the dimensionless distance $2h/c = 0.8$ between the symmetrical wings characterizing the overall geometry of the prototype depicted in figure 3, are not arbitrary. Indeed, the aerator system shown in figure 3 has been designed choosing values of α and h/c that maximize the value of the favourable pressure gradient $\beta(\alpha)$ and minimize the value of the pressure coefficient at the leading edge of the wing $Cp(x/c = 0)$ -see equations 10 and 12- while keeping the value of the drag coefficient as small as possible i.e., preventing the separation of the boundary layer that would take place if the maximum value of the adverse pressure gradient was larger than a certain threshold. For the case of the NACA 0012 airfoils used to buid the prototype depicted in figure 3, the numerical results in figure 4 reveal that $\beta(\alpha)$ and $-C_p(x/c = 0)$ increase when either α increases or h/c decreases. However, the maximum value of the adverse pressure gradient, calculated as the slope of the function $-C_p(x/c)$ at the yellow circles indicated in figures 4b-c also increases when either α increases or h/c

decreases. It is known that the stall angle for an isolated ($h/c \to \infty$) NACA 0012 airfoil, is $\alpha^* \simeq 12^o$ (see for instance [29]), and also that stall is provoked by the separation of the boundary layer. Using the boundary integral code described in [27,28], we have calculated the value of the maximum adverse pressure gradient for an isolated NACA 0012 airfoil at an angle of attack $\alpha = \alpha^* \simeq 12^o$, finding that $dC_p/d\bar{s} \simeq 200$. Then, in order to ensure that the boundary layer does not separate, in the present design we have chosen a value of α which is as large as posible and a value of h/c which is as small as possible, and such that the maximum value of the adverse pressure gradient is below 100, see figure 4d. These are the reasons justifying the values of the geometrical dimensions provided in table 1 defining the prototype depicted in figure 3. In addition, the wings, connected to the rotating axis through rigid metal tubes, are hollow, as well as the shaft through which the gas is supplied, as it can be appreciated in figure 3. In this way, the gas can flow from the pressurized reservoir through the N tubes of inner diameter d_t and length ℓ_t placed at the leading edge of the symmetrical NACA 0012 airfoils composing each of the wings, see figures 3 and 5a. The values of d_t and ℓ_t depicted in table 1 are chosen so that the pressure drop through each of the tubes is large enough to ensure that bubbles are produced at constant gas flow rate conditions [14].

Moreover, the two couples of symmetrical wings are also connected by NACA0012 airfoils in order to prevent the formation of wing-tip vortices, which increase the drag force and also decrease the effective angle of attack of the airfoils, thus reducing the value of β and, hence, of the favourable pressure gradient (see figure 4a). In addition, since the tips of the wings (i.e. the end parts of the wings in the spanwise direction) are connected, the flow around the airfoils is nearly two-dimensional. Therefore, the two-dimensional boundary integral code described in [27,28] can be used to calculate the values of $C_p(x/c)$ and β shown in figure 4.

The bubbling device is placed inside a plexiglass reservoir with a 1 meter-sided square base filled with tap water, see figure 5a. The visualization of the bubble formation process is extremely challenging and not straightforward at all because the distance from the leading edge of the wing to one of the transparent sides of the tank, where a high speed camera is located, is $\simeq 0.35$ m -see figure 5b-d. Then, since the typical diameter of the bubbles is much smaller, typically, $d_b \sim 10^{-4}$ m, the ratio between the focal distance and d_b is $\sim 10^3$. Moreover, in order to accurately describe the bubble formation process and since $f_b \sim 10^4$ Hz and $\Omega R \sim 2$ ms^{-1}, our Phantom v710 high speed camera is operated, depending on the angular velocity Ω, at 5×10^4-7.5×10^4 f.p.s. (frames per second) and with a very small

exposure time of 10^{-5} s. This latter restriction forced us to operate two cold light sources (Schott KL2500) at their maximum power and to introduce their optical fibre cables inside the water tank, as it can be appreciated in figure 5d. In addition, the pixel size of the high speed camera is $20\,\mu m$, and since 6-8 pixels per bubble are needed to minimize the measurement errors, the images need to be magnified by a factor of 2-3. This requirement, together with the fact that bubbles are produced at a distance of ~ 0.35 m from the camera -see figure 5b-d, led us to make use of the long-distance microscope Questar QM 100 depicted in figure 5c-d, which possesses a depth of field in water of ~ 200 μm.

The values of both f_b and d_b are determined from the analysis of the recorded images: the bubbling frequency is measured as the inverse of 1/5 of the time required for 5 bubbles to cross an imaginary line, whereas bubble diameter is the averaged value of the major and minor axes of the ellipse that best fits the recorded bubble shapes. Experiments are performed by controlling the value of the two governing parameters namely, the angular velocity Ω, which is varied between 45 to 80 r.p.m. (revolutions per minute) and the value of the gas overpressure within the hollow wings, Δp_g, which is measured using a digital manometer (Digitron 2003P) and is varied between 8000 Pa and 25000 Pa using a high precision valve (Rexroth). All the results presented here correspond to experiments performed with tap water: no surfactants were added.

Figure 6 compares the water tank before and after the aerator described here was operated during 2 minutes at $\Omega = 2\pi$ rad/s with $\Delta p_g = 1.25 \times 10^4$ Pa. Figure 6 reveals the change in the brightness of water caused by the presence of $d_b \sim 200\,\mu m$ microbubbles which, thanks to the agitation introduced by the rotating wings, are uniformfly distributed within the reservoir. The detailed bubble formation process, recorded in the plane π perpendicular to the high speed camera (see figure 5b), is depicted in figures 7a-d. This figure shows how bubbles grow and detach downstream the injection orifices and, also, the qualitative effect of varying either Ω or Δp_g. As expected from the results shown in[27] d_b increases when Δp_g increases, i.e., when the gas flow rate increases. Figure 7 also shows that the bubbling frequency increases and the diameters of the bubbles produced decrease when Ω is increased for a given value of Δp_g. Let us point out that we unsuccessfully tried to improve the quality of the images depicted in figure 7. This is because the depth of field of the long-distance microscope Questar QM 100 depicted in figure 5c-d is ~ 1000 times smaller than the focal distance. In addition, as it was explained in the paragraph above, the correct

illumination of the region near the gas injection orifice where bubbles are produced, is also extremely challenging. Figure 7 also shows that, indeed, the present design prevents the coalescence of consecutive bubbles right after they are issued from the gas injection orifice. However, from the analysis of the images recorded we cannot ensure that bubble coalescence does not take place further downstream, an issue that could be avoided adding surfactants.

Figure 8 compares the experimental values of f_b and d_b with those predicted using equations (10) once $\beta(\alpha)$ is calculated by means of the numerical boundary integral code described in[27,28]. Figure 8, which includes the experimental data of the present study, the data reported in [26] -see the sketch in figure 1b- and also the experimental data reported in [27] -see the sketch in figure 1c, reveals that equations in (10) accurately predict the observations, validating our physical description.

Notice that the analysis of the results depicted in figure 8 reveals that the diameters of the bubbles produced are not smaller than 120 μm. This is due to the fact that, because of experimental limitations, we have not been able to analyse the cases corresponding to wing speeds larger than $\Omega R = 2\ \mathrm{m \cdot s^{-1}}$. Let us also point out here that figure 8 only includes the experimental data for which the bubbles are formed under constant flow rate conditions. This condition is only verified when the gas pressure drop along the injection tube is substantially larger than the capillary pressure fluctuations $\sim O(4\sigma/d_t)$ namely, when:

$$\frac{\Delta p_g - \rho g H + \rho \left(\Omega R\right)^2 C_p \left(x/c = 0\right)/2}{4\sigma/d_t} \gtrsim C_1 \tag{14}$$

with $C_1 \sim 2.5$ an adjusted constant, see[30] for details. While we have checked that bubbles can be produced for values of Δp_g smaller than the ones indicated by equation (14), we have also observed that, under these conditions, the bubble formation process is no longer periodic. Therefore, this other regime of bubble generation is not so relevant for applications because the diameters of the bubbles produced in this way are no longer uniform.

The good agreement between measurements and predictions depicted in figure 8 indicate that equations (10) can be used to predict bubble sizes and bubbling frequencies for angular velocities larger than those investigated here. Therefore, taking into account that the present prototype incorporates 144 injection sites, the results of equations

(10) and (11) permit us to conclude that the aerator depicted in figures 3 and 5 could be used to inject a gas flow rate of 1.5 $l \cdot h^{-1}$ of bubbles with a diameter of $d_b = 50\,\mu m$ if the angular velocity was fixed to $\Omega = 170$ r.p.m.. Clearly, the injected gas flow rate could be increased by simply adding more wings and more aeration sites.

4 | CONCLUSIONS

In this contribution we have designed and tested a new type of aerator which is capable to generate, in a controlled and massive way, non-coalescing monodisperse microbubbles. The present design is motivated by the fact that the pressure gradient existing at the leading edge of an airfoil at an angle of attack and in relative motion with a liquid is far larger than the hydrostatic pressure gradient. Then, the aerator consists of hollow wings that rotate around a hollow shaft and these wings also incorporate N injection tubes through which the air flows from a pressurized gas reservoir to their leading edges. Using the theoretical framework provided in [26,27], we have deduced closed algebraic expressions that predict well the bubbling frequencies and also the bubble diameters. The prototype presented here is, in addition, efficient from an energetically point of view because it prevents the separation of the boundary layer and also because the gas is injected at the leading edge of the airfoils composing the wings, where the liquid pressure is appreciably smaller than the hydrostatic pressure. This aeration system can be easily adapted to satisfy the specific gas demands of different processes in chemical industry: for example, by adding more wings or more gas injection orifices, it could be used in bioreactors or in water treatment plants.

References

1 A. Agarwal, W. Jern Ng, and Y. Liu. Principle and applications of microbubble and nanobubble technology for water treatment. *Chemosphere*, 84(9):1175 – 1180, 2011. ISSN 0045-6535.

2 D. Rosso, L. E. Larson, and M. K. Stenstrom. Aeration of large-scale municipal wastewater treatment plants: State of the art. *Water Science and Technology*, 57(7):973–978, 2008. ISSN 02731223. doi: 10.2166/wst.2008.218.

3 P. Li, H. Tsuge, and K. Itoh. Oxidation of dimethyl sulfoxide in aqueous solution using microbubbles. *Industrial & Engineering*

Chemistry Research, 48(17):8048–8053, 2009.

4 M. D. Bredwell and R. M. Worden. Mass-transfer properties of microbubbles. 1. experimental studies. *Biotechnology Progress*, 14(1):31–38, 1998.

5 A. M. Henstra, J. Sipma, A. Rinzema, and A. JM. Stams. Microbiology of synthesis gas fermentation for biofuel production. *Current Opinion in Biotechnology*, 18(3):200 – 206, 2007.

6 F. Garcia-Ochoa and E. Gomez. Bioreactor scale-up and oxygen transfer rate in microbial processes: an overview. *Biotechnology advances*, 27(2):153–76, 2009. ISSN 1873-1899. doi: 10.1016/j.biotechadv.2008.10.006. URL http://www.ncbi.nlm.nih.gov/pubmed/19041387.

7 S. Khuntia, K. M. Subrata, and G. Pallab. Microbubble-aided water and wastewater purification: a review. *Rev. Chem. Eng.*, 28:191?221, 2012.

8 P.K. Sharma, M.J. Gibcus, H.C. van der Mei, and H.J. Busscher. Influence of fluid shear and microbubbles on bacterial detachment from a surface. *Appl. Environ. Microbiol.*, 71:3668?3673, 2005.

9 S. Yoshizawa, T. Ikeda, A. Ito, R. Ota, S. Takagi, and Y. Matsumoto. High intensity focused ultrasound lithotripsy with cavitating microbubbles. *Medical and Biological Engineering and Computing*, 47(8):851–860, 2009. ISSN 01400118. doi: 10.1007/s11517-009-0471-y.

10 K. Ferrara, R. Pollard, and M. Borden. Ultrasound microbubble contrast agents: Fundamentals and application to gene and drug delivery. *Annual Review of Biomedical Engineering*, 9:415–447, 2007.

11 Rajeev P. and Subrata K. M. Microbubble generation and microbubble-aided transport process intensification: A state-of-the-art report. *Chemical Engineering and Processing: Process Intensification*, 64:79 – 97, 2013.

12 Tatek Temesgen, Thi Thuy Bui, Mooyoung Han, Tschung il Kim, and Hyunju Park. Micro and nanobubble technologies as a new horizon for water-treatment techniques: A review. *Advances in Colloid and Interface Science*, 246:40 – 51, 2017. ISSN 0001-8686.

13 J. Rodríguez-Rodríguez, A. Sevilla, C. Martínez-Bazán, and J. M. Gordillo. Generation of microbubbles with applications to industry and medicine. *Annual Review of Fluid Mechanics*, 47:405–429, 2015.

14 H N Oguz and A Prosperetti. Dynamics of Bubble-Growth and Detachment from a Needle. *Journal of Fluid Mechanics*, 257:111–145, 1993. ISSN 0022-1120. doi: 10.1017/S0022112093003015.

15 F.J. Higuera and A. Medina. Injection and coalescence of bubbles in a quiescent inviscid liquid. *European Journal of Mechanics - B/Fluids*, 25(2):164 – 171, 2006. ISSN 0997-7546.

16 L. Zhang and M. Shoji. Aperiodic bubble formation from a submerged orifice. *Chemical Engineering Science*, 56(18):5371 – 5381, 2001.

17 A.M. Ganan-Calvo and J.M. Gordillo. Perfectly monodisperse microbubbling by capillary flow focusing. *Physcal Review Letters*, 87:274501, 2001.

18 P. Garstecki, I. Gitlin, W. DiLuzio, G. M. Whitesides, E. Kumacheva, and H. A. Stone. Formation of monodisperse bubbles in a microfluidic flow-focusing device. *Applied Physics Letters*, 85:2649–2651, 2004.

19 T. Fu and Y. Ma. Bubble formation and breakup dynamics in microfluidic devices: A review. *Chemical Engineering Science*, 135:343–372, 2014. ISSN 00092509. doi: 10.1016/j.ces.2015.02.016.

20 M. Yasuno, S. Sugiura, S. Iwamoto, M. Nakajima, A. Shono, and K. Satoh. Monodispersed microbubble formation using microchannel technique. *AIChE Journal*, 50(12):3227–3233, 2004.

21 J. H. Xu, S. W. Li, G. G. Chen, and G. S. Luo. Formation of monodisperse microbubbles in a microfluidic device. *AIChE Journal*, 52(6):2254–2259, 2006.

22 K. Hettiarachchi, E. Talu, M.L. Longo, P.A Dayton, and A.P. Lee. On-chip generation of microbubbles as a practical technology for manufacturing contrast agents for ultrasonic imaging. *Lab Chip*, 7:463–468, 2007.

23 E. Castro-Hernández, W. van Hoeve, D. Lohse, and J.M. Gordillo. Microbubble generation in a co-flow device operated in a new regime. *Lab Chip*, 11:2023–2029, 2011.

24 F. Campo-Cortés, G. Riboux, and J. M. Gordillo. The effect of contact line pinning favors the mass production of monodisperse microbubbles. *Microfluidics and Nanofluidics*, 20:21:405–429, 2016.

25 J. M. Gordillo. Axisymmetric bubble collapse in a quiescent liquid pool. Part I: Theory and numerical simulations. *Phys. Fluids*, 20:112103, 2008.

26 A. Evangelio, F. Campo-Cortés, and J.M. Gordillo. Pressure gradient induced generation of microbubbles. *Journal of Fluid Mechanics*, 778:653–668, 2015. ISSN 0022-1120. doi: 10.1017/jfm.2015.408.

27 E. S. Quintero, A. Evangelio, and J. M. Gordillo. Production of monodisperse microbubbles avoiding microfluidics. *Journal of Fluid Mechanics*, 846:R3, 2018. doi: 10.1017/jfm.2018.312.

28 Enrique S. Quintero. *Fragmentación de corrientes gaseosas y de masas líquidas en flujos naturales y de interés tecnológico*. PhD thesis, University of Seville, 2019.

29 I. H. Abbot and A. E. Von Doenhoff. *Theory of wing sections. Including a summary of airfoil data*. Dover Publications, Inc., 1959.

30 J. M. Gordillo, A. Sevilla, and C. Martínez-Bazán. Bubbling in a co-flow at high Reynolds numbers. *Physics of Fluids*, 19(7): 077102, 2007.

List of Figures

1 (a) Sketch showing the bubble formation process using the straightforward approach of injecting a gas through a vertical tube in a stagnant liquid pool. Here, $|\nabla p| = \rho g$. (b) Generation of microbubbles using the microfluidic device described in [26]. In this case, $|\nabla p| = \rho U^2/L$. (c) Generation of microbubbles at the leading edge of airfoils following the procedure described in [27]. In this case, $|\nabla p| = \rho\beta(\alpha)\, U_\infty^2/c$. From now on, the value of L will be fixed here to $L = 10^{-3}$ m. 17

2 The liquid pressure distribution along the surface of a symmetric airfoil, with $\alpha \neq 0$ indicating the angle of attack, is such that there exist regions with a favourable ($dp/ds < 0$) or an adverse ($dp/ds > 0$) pressure gradient, with s indicating the arc length. The maximum and minimum values of the liquid pressure are reached, respectively, at the stagnation point and at the suction peak. The leading edge is in between these two points, which are located very close to each other, this fact explaining the very large value of the favourable pressure gradient existing at the leading edge of the airfoil. The pressure gradient is adverse ($dp/ds > 0$) downstream the suction peak. 18

3 Sketch of the aeration system indicating its main geometrical dimensions as well as the two governing parameters, namely, the angular speed Ω and the gas flow rate per orifice, Q_g. N indicates the number of gas injection sites. 19

4 Numerical values of $C_p(x/c, \alpha, h/c)$ and of $\beta(\alpha, h/c)$ calculated using the boundary integral code described in [27,28] for the type of NACA 0012 airfoils used in the present design, which solves the Laplace equation for the velocity potential subjected to the impenetrability condition at the airfoils composing the wing and the Euler-Bernoulli equation to calculate the pressure. (a) The value of $\beta(\alpha, h/c)$, with $2h/c$ indicating the dimensionless distance between the symmetrically-placed airfoils depicted in figure 3, increases with α and for decreasing values of h/c. (b) Influence of α on $C_p(x/c)$ for $h/c = 1$: notice that the value of the pressure coefficient at the leading edge of the airfoil decreases with α. (c) Influence of h/c on $C_p(x/c)$ for $\alpha = 8^o$: notice that the value of the pressure coefficient at the leading edge of the airfoil decreases when the value of h/c is decreased. In (b)-(c), dashed lines indicate values at the pressure side of the airfoil and the yellow dots on the curves indicate the position where the value of the adverse pressure gradient is maximum. (d) The values of the maximum adverse pressure gradient increase with α and for decreasing values of h/c. 20

5 (a) This figure shows the materialization of the aerator sketched in figure 3. The wings, fabricated using ABS (Acrylonitrile Butadiene Styrene), are connected through the shaft to a trifasic electric motor, which provides with the necessary torque to make the aeration system rotate. The air flows through the hollow shaft from the pressurized gas reservoir to the rotating wings, where the gas injection tubes are located -see figure 1c and the inset in figure 3. (b) A sketch of the experimental setup is depicted in this figure: the camera is placed perpendicular to the water tank wall and to the focus plane, π. The zoomed view shows the gas injection orifices; a letter is added with the only purpose of identifying the micron-sized spatial region visualized in the videos. Notice that the focal distance is $\sim 10^3$ times larger than the area visualized in the recorded images. (c) The high speed camera, coupled with a long-distance microscope, is located outside the water tank and placed at a focal distance of, approximately, 0.35 m from the plane π sketched in (b). Figure (d) shows how close to the rotating wing the fibre-optic cables must be placed in order to appropriately illuminate the region where the bubble formation process takes place. 21

6 Images showing the water tank before (a) and after (b) the aeration device is operated during 2 minutes at $\Omega = 2\pi$ rad/s. The appreciable change in the brighness of water is caused by the light dispersed by the $d_b \sim 200\mu m$ bubbles uniformly distributed along tank, which is filled with tap water without surfactants. 22

7 (a)-(b): Effect of the variation of Δp_g on the diameters of the bubbles produced, d_b, for a fixed value of the angular velocity, $\Omega R = U_\infty = 1.87\,\mathrm{m \cdot s^{-1}}$. In (a) $\Delta p_g = 1.25 \times 10^4$ Pa and in (b), $\Delta p_g = 2.5 \times 10^4$ Pa. (c)-(d): Effect of the variation of $\Omega R = U_\infty$ on the diameters of the bubbles produced, d_b, for a constant value of the gas injection pressure, $\Delta p_g = 1.6 \times 10^4$ Pa. In (c), $\Omega R = U_\infty = 1.03\,\mathrm{m \cdot s^{-1}}$ whereas in (d) $\Omega R = U_\infty = 1.87\,\mathrm{m \cdot s^{-1}}$. This figure also illustrates the way the diameters of the bubbles produced are measured. The black area in the experimental images represents a fraction of the letter depicted in figure 5b, which helps identify the spatial position of the recorded area and also helps enhance the contrast between the bubble and the background. 22

8 The experimental values of both f_b and d_b are compared with the predictions given in equation (10). Here, we do not only include the present experimental measurements (cyan squares, $U_\infty = \Omega R$, $c = 0.1$ m), but also the ones reported in [27] (where $c = 0.3$ m, see the red rectangle) and in [26] (magenta diamonds, see figure 1b, where $U_\infty = U$, $L\,\beta(\alpha)/c = 1.5$, being $\beta(\alpha) = 1.5$ the non-dimensional pressure gradient in [26]). Notice we have used the characteristic length $L = 10^{-3}$ m to non-dimensionalize d_b and, therefore, the experimental results in [26,27] can be directly compared with those measured here. The main source of the error in our experimental data is associated with the limited spatial resolution, which introduce an uncertainty of ~ 4 pixels$\sim 30\,\mu$m in the measured values of d_b. 23

Dimensions	Values
Chord c [m]	0.1
Span b [m]	0.2
Gap $2h$ [m]	0.08
Distance of the midplane of the wings from the rotation axis R [m]	0.25
Angle of attack α [deg]	7
Tube length ℓ_t [m]	0.03
Tube diameter d_t [$\times 10^{-6}$ m]	50
Number of tubes N	144
Distance between neighbouring gas injection orifices e [m]	0.005

TABLE 1 Values of the different geometrical dimensions characterizing the bubble maker depicted in figures 3 and 5b. The cross section of the wings are NACA 0012 airfoils.

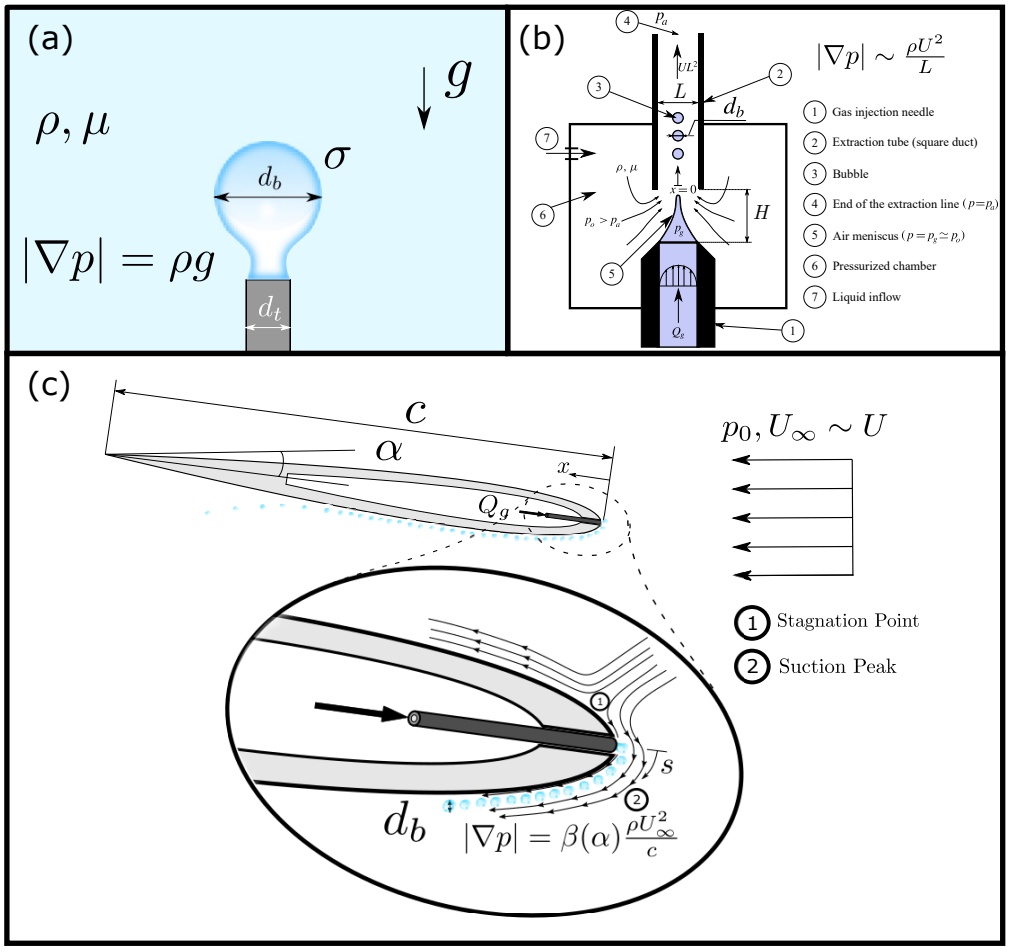

FIGURE 1 (a) Sketch showing the bubble formation process using the straightforward approach of injecting a gas through a vertical tube in a stagnant liquid pool. Here, $|\nabla p| = \rho g$. (b) Generation of microbubbles using the microfluidic device described in [26]. In this case, $|\nabla p| = \rho U^2/L$. (c) Generation of microbubbles at the leading edge of airfoils following the procedure described in [27]. In this case, $|\nabla p| = \rho\beta(\alpha) U_\infty^2/c$. From now on, the value of L will be fixed here to $L = 10^{-3}$ m.

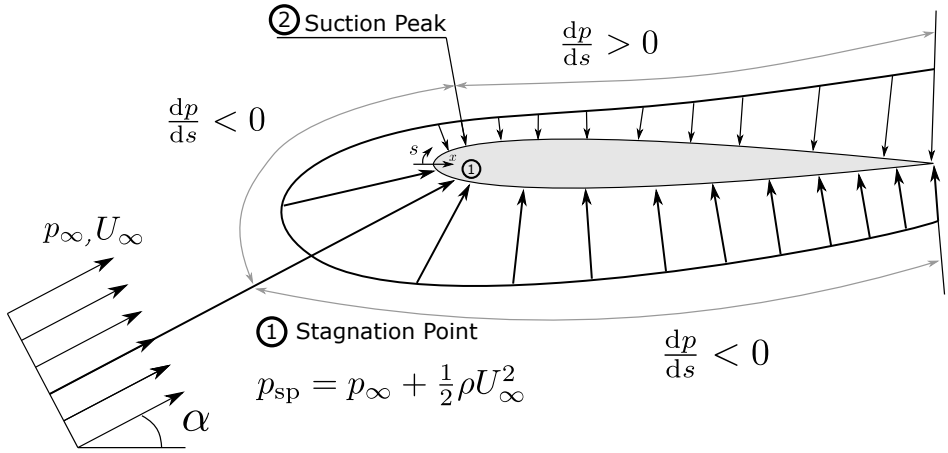

FIGURE 2 The liquid pressure distribution along the surface of a symmetric airfoil, with $\alpha \neq 0$ indicating the angle of attack, is such that there exist regions with a favourable ($dp/ds < 0$) or an adverse ($dp/ds > 0$) pressure gradient, with s indicating the arc length. The maximum and minimum values of the liquid pressure are reached, respectively, at the stagnation point and at the suction peak. The leading edge is in between these two points, which are located very close to each other, this fact explaining the very large value of the favourable pressure gradient existing at the leading edge of the airfoil. The pressure gradient is adverse ($dp/ds > 0$) downstream the suction peak.

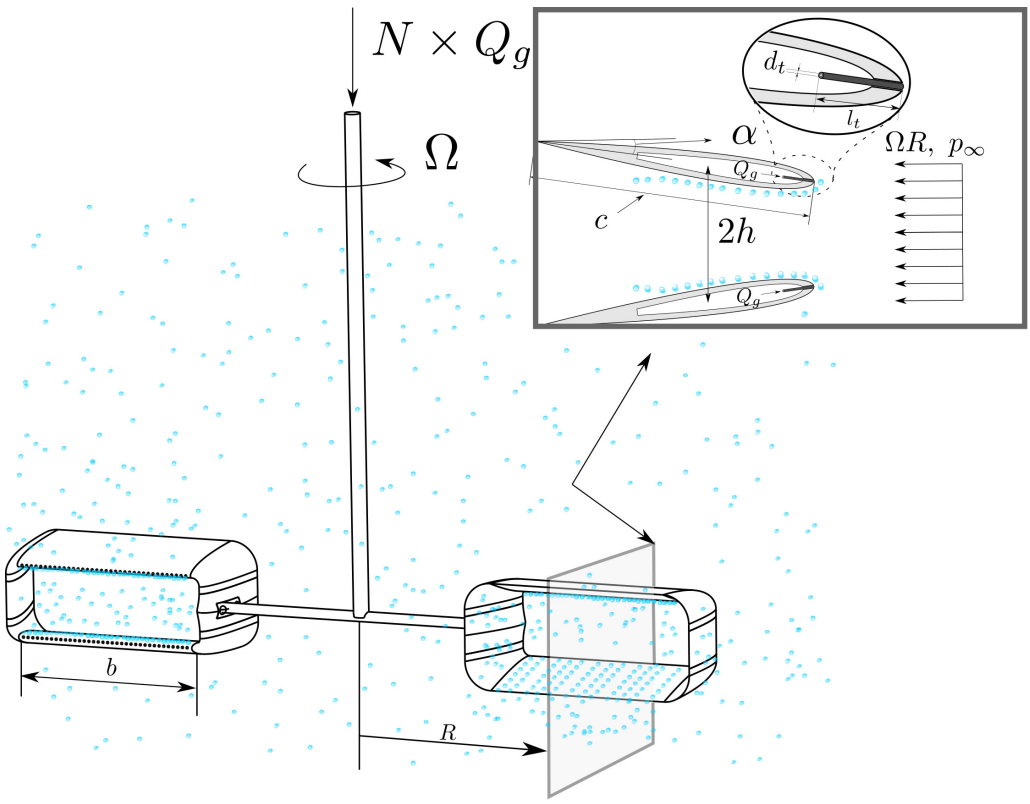

FIGURE 3 Sketch of the aeration system indicating its main geometrical dimensions as well as the two governing parameters, namely, the angular speed Ω and the gas flow rate per orifice, Q_g. N indicates the number of gas injection sites.

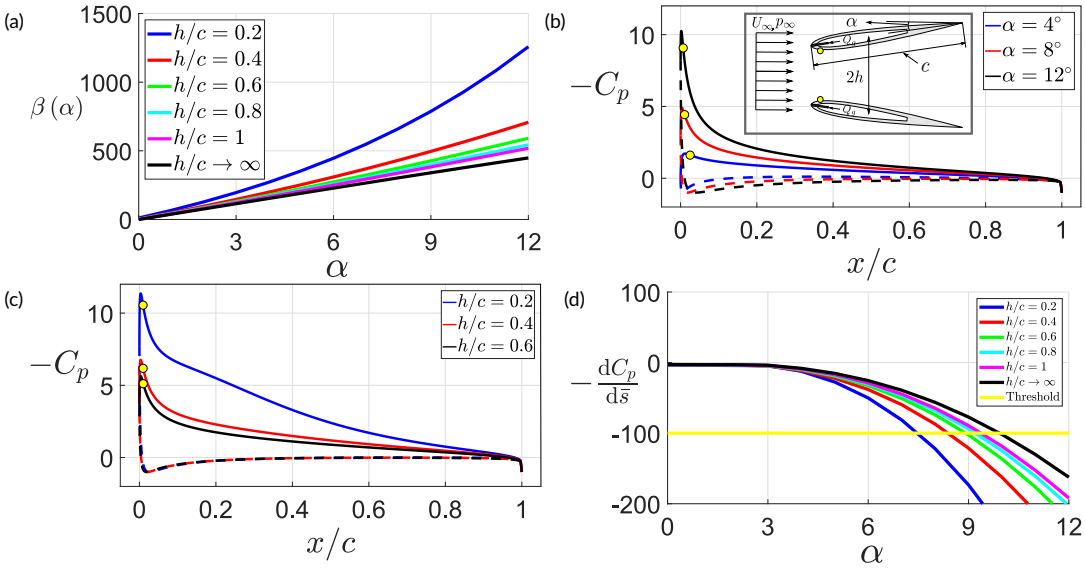

FIGURE 4 Numerical values of $C_p(x/c, \alpha, h/c)$ and of $\beta(\alpha, h/c)$ calculated using the boundary integral code described in[27,28] for the type of NACA 0012 airfoils used in the present design, which solves the Laplace equation for the velocity potential subjected to the impenetrability condition at the airfoils composing the wing and the Euler-Bernoulli equation to calculate the pressure. (a) The value of $\beta(\alpha, h/c)$, with $2h/c$ indicating the dimensionless distance between the symmetrically-placed airfoils depicted in figure 3, increases with α and for decreasing values of h/c. (b) Influence of α on $C_p(x/c)$ for $h/c = 1$: notice that the value of the pressure coefficient at the leading edge of the airfoil decreases with α. (c) Influence of h/c on $C_p(x/c)$ for $\alpha = 8^o$: notice that the value of the pressure coefficient at the leading edge of the airfoil decreases when the value of h/c is decreased. In (b)-(c), dashed lines indicate values at the pressure side of the airfoil and the yellow dots on the curves indicate the position where the value of the adverse pressure gradient is maximum. (d) The values of the maximum adverse pressure gradient increase with α and for decreasing values of h/c.

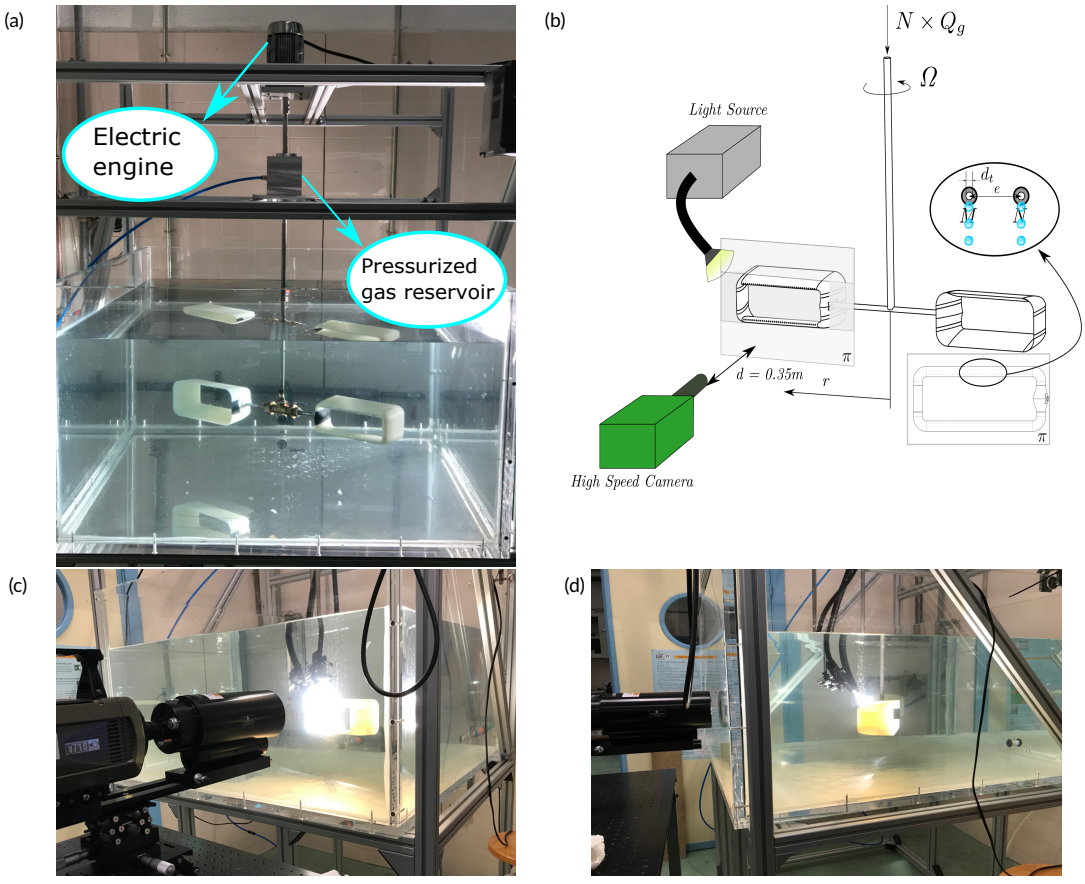

FIGURE 5 (a) This figure shows the materialization of the aerator sketched in figure 3. The wings, fabricated using ABS (Acrylonitrile Butadiene Styrene), are connected through the shaft to a trifasic electric motor, which provides with the necessary torque to make the aeration system rotate. The air flows through the hollow shaft from the pressurized gas reservoir to the rotating wings, where the gas injection tubes are located -see figure 1c and the inset in figure 3. (b) A sketch of the experimental setup is depicted in this figure: the camera is placed perpendicular to the water tank wall and to the focus plane, π. The zoomed view shows the gas injection orifices; a letter is added with the only purpose of identifying the micron-sized spatial region visualized in the videos. Notice that the focal distance is $\sim 10^3$ times larger than the area visualized in the recorded images. (c) The high speed camera, coupled with a long-distance microscope, is located outside the water tank and placed at a focal distance of, approximately, 0.35 m from the plane π sketched in (b). Figure (d) shows how close to the rotating wing the fibre-optic cables must be placed in order to appropriately illuminate the region where the bubble formation process takes place.

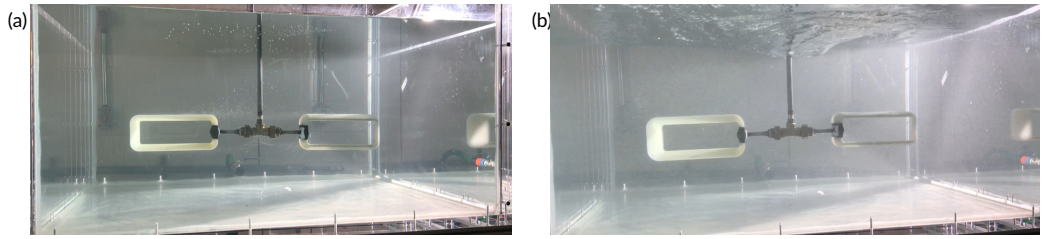

FIGURE 6 Images showing the water tank before (a) and after (b) the aeration device is operated during 2 minutes at $\Omega = 2\pi$ rad/s. The appreciable change in the brighness of water is caused by the light dispersed by the $d_b \sim 200\mu m$ bubbles uniformly distributed along tank, which is filled with tap water without surfactants.

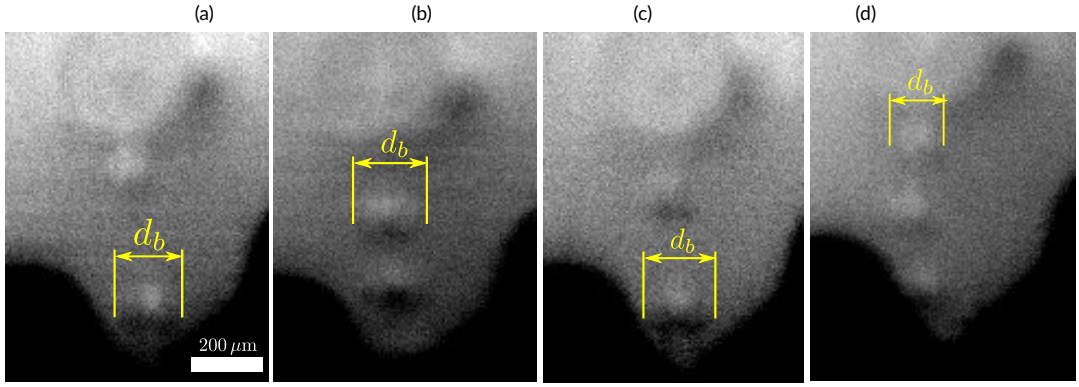

FIGURE 7 (a)-(b): Effect of the variation of Δp_g on the diameters of the bubbles produced, d_b, for a fixed value of the angular velocity, $\Omega R = U_\infty = 1.87\,\mathrm{m}\cdot\mathrm{s}^{-1}$. In (a) $\Delta p_g = 1.25 \times 10^4$ Pa and in (b), $\Delta p_g = 2.5 \times 10^4$ Pa. (c)-(d): Effect of the variation of $\Omega R = U_\infty$ on the diameters of the bubbles produced, d_b, for a constant value of the gas injection pressure, $\Delta p_g = 1.6 \times 10^4$ Pa. In (c), $\Omega R = U_\infty = 1.03\,\mathrm{m}\cdot\mathrm{s}^{-1}$ whereas in (d) $\Omega R = U_\infty = 1.87\,\mathrm{m}\cdot\mathrm{s}^{-1}$. This figure also illustrates the way the diameters of the bubbles produced are measured. The black area in the experimental images represents a fraction of the letter depicted in figure 5b, which helps identify the spatial position of the recorded area and also helps enhance the contrast between the bubble and the background.

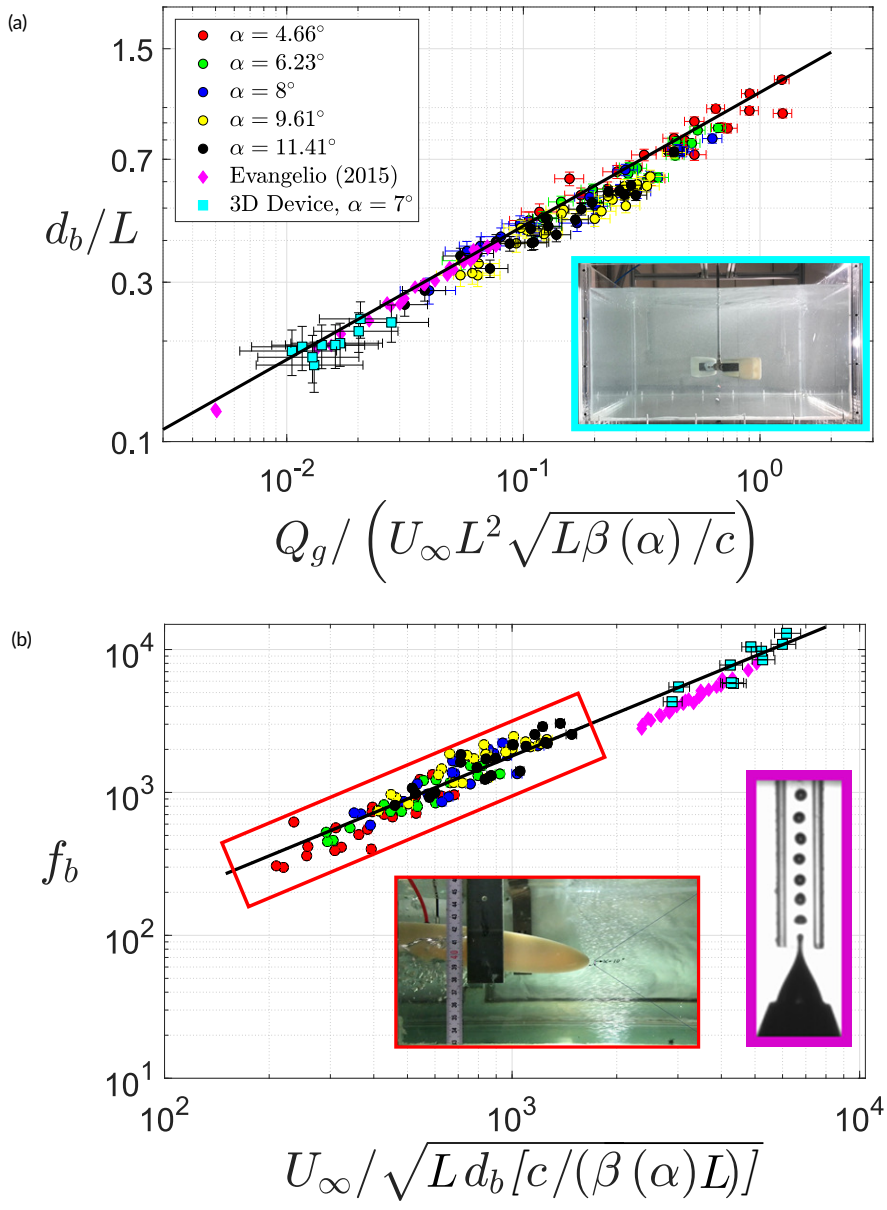

FIGURE 8 The experimental values of both f_b and d_b are compared with the predictions given in equation (10). Here, we do not only include the present experimental measurements (cyan squares, $U_\infty = \Omega R$, $c = 0.1$ m), but also the ones reported in [27] (where $c = 0.3$ m, see the red rectangle) and in [26] (magenta diamonds, see figure 1b, where $U_\infty = U$, $L\beta(\alpha)/c = 1.5$, being $\beta(\alpha) = 1.5$ the non-dimensional pressure gradient in [26]). Notice we have used the characteristic length $L = 10^{-3}$ m to non-dimensionalize d_b and, therefore, the experimental results in [26,27] can be directly compared with those measured here. The main source of the error in our experimental data is associated with the limited spatial resolution, which introduce an uncertainty of ~ 4 pixels$\sim 30\,\mu$m in the measured values of d_b.